Chemical Science

Accepted Manuscript

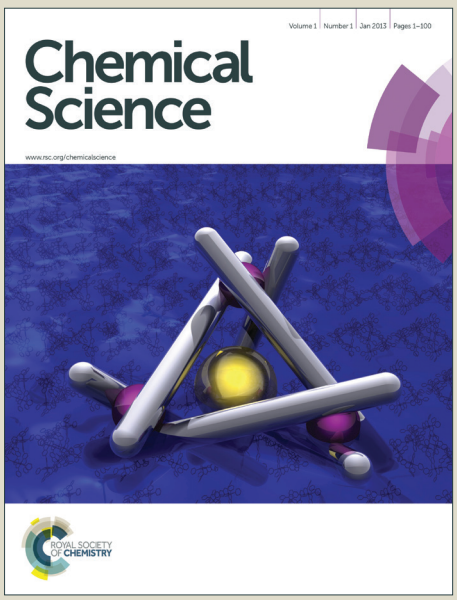

ROYAL SOCIETY OF CHEMISTRY

www.rsc.org/chemicalscience

Chemical Science

Chemical Science

Dynamic Article Links ►

Cite this: DOI: 10.1039/c0xx00000x

www.rsc.org/xxxxxx

EDGE ARTICLE

Roles of carboxylate donors in O-O bond scission of peroxodiiron(III) to high-spin oxodiiron(IV) with a new carboxylate-containing dinucleating ligand

Masahito Kodera,*[a] Tomokazu Tsuji,[a] Tomohiro Yasunaga,[a] Yuka Kawahara,[a] Tomoya Hirano,[a] Yutaka Hitomi,[a] Takashi Nomura,[b] Takashi Ogura,[b] Yoshio Kobayashi,[c] P. K. Sajith,[d] Yoshihito Shiota[d] and Kazunari Yoshizawa[d]

Received (in XXX, XXX) Xth XXXXXXXXX 20XX, Accepted Xth XXXXXXXXX 20XX

DOI: 10.1039/b000000x

Dioxygen activation proceeds via O-O bond scission of peroxodiiron(III) to high-spin oxodiiron(IV) in soluble methane monooxygenase (sMMO). Recently, we have shown that reversible O-O bond scission of peroxodiiron(III) to high-spin oxodiiron(IV) is attained with a bis-tpa type dinucleating ligand, 6-hpa. In this study, a new carboxylate-containing dinucleating ligand, 1,2-bis[2-(*N*-2-pyridylmethyl-*N*-glycinylmethyl)-6-pyridyl]ethane (H_2BPG_2E) and its μ-oxodiaquadiiron(III) complexes $[Fe_2(\mu\text{-}O)(H_2O)_2(BPG_2E)]X_2$ [X = ClO_4 (**2a**) or OTf (**2b**)] were synthesized to mimic a common carboxylate-rich coordination environment in O_2-activating non-heme diiron enzymes including sMMO. The crystal structures of **2a** and **2b** revealed that BPG_2E prefers a syn-diaqua binding mode. **2b** catalyzed the epoxidation of alkenes with H_2O_2. A new purple species was formed upon reaction of **2b** with H_2O_2, and characterized by the elemental analysis and spectral and kinetic studies. These clearly showed that the purple species was a μ-oxo-μ-peroxodiiron(III), and converted to high-spin μ-oxodioxodiiron(IV) via rate-determining reversible O-O bond scission. In comparison of BPG_2E with 6-hpa, it is shown that the carboxylate donor stabilizes the Fe-O-O-Fe structure of peroxo complex due to the structural effect to retard the O-O bond scission. This may shed light on roles of the carboxylate donors in the dioxygen activation of the non-heme diiron enzymes.

Introduction

Peroxodiiron(III) and high-spin oxodiiron(IV) are formed as key intermediates in dioxygen activation of O_2-activating non-heme diiron enzymes,[1] including soluble methane monooxygegenase (sMMO),[2] toluene/*o*-xylene monooxygenase (ToMO),[3] toluene monooxygenase (TMO),[4] deoxyhypusine hydroxylase (DOHH).[5] The diiron centers are bound at a common carboxylate-rich site. However, reactivity and spectral features of the intermediates vary according to the enzyme. In sMMO, the peroxo intermediate P is converted to the high-spin oxodiiron(IV) active species Q.[2,6] In TMO and ToMO, the peroxo species are unstable, showing almost no electronic absorption feature with unique Mössbauer parameters.[3,7] In DOHH, the peroxodiiron(III) is a resting form, stable without substrate, and upon addition of substrate, rapidly oxidizes it.[5] The carboxylate donor may control reactivity of the key intermediates, but the roles in the dioxygen activation and the substrate oxidation have not been clarified yet.

Some peroxodiiron(III) complexes with carboxylate-containing ligands mimicking carboxylate-rich sites have been reported.[8] Que reported the formation of a peroxodiiron(III) with 2,6-di-mesitylbenzoate.[9] With a less sterically hindered ligand, 2,6-di-*p*-tolylbenzoate, Lippard detected di-μ-oxodiiron(III)(IV).[10] These species, however, are so unstable that it is difficult to clarify the O_2-activation mechanism. Suzuki determined crystal structures of μ-oxo-μ-peroxodiiron(III) of a carboxylate-containing ligand 6-Me_2-BPP $[Fe_2(\mu\text{-}O)(\mu\text{-}O_2)(6\text{-}Me_2\text{-}BPP)_2]$ and its μ-hydroxo form, both of which, however, do not undergo the O-O bond scission to show no reactivity for the substrate oxidation.[11] Lippard reported generation of a peroxo species upon reaction of μ-oxodiaquadiiron(III) of a carboxylate-containing dinucleating ligand, H_2BPG_2DEV, $[Fe_2(\mu\text{-}O)(H_2O)_2(BPG_2DEV)](ClO_4)_2$ with H_2O_2, which shows low epoxidation activity.[12] Thus, the formation of high-spin diiron(IV) and the efficient catalytic oxidation of hydrocarbons have never attained by peroxo complexes of carboxylate-containing ligands.

Recently, we have shown that efficient catalytic epoxidation of various alkenes with H_2O_2[13a] and spectroscopic characterization of peroxodiiron(III) and high-spin oxodiiron(IV) generated via the reversible O-O bond scission in the H_2O_2 activation[13b] are attained using μ-oxodiaquadiiron(III) complex of a bis-tpa dinucleating ligand 6-hpa $[Fe_2(\mu\text{-}O)(H_2O)_2(6\text{-hpa})](ClO_4)_4$ (**1**), where 6-hpa is 1,2-bis[2-[bis(2-pyridylmethyl)aminomethyl]-6-pyridyl]ethane (see Scheme 1(A)). This is a promising functional model capable of reproducing conversion of the peroxo intermediate P to the active species Q, high-spin oxodiiron(IV), in the catalytic O_2-activation cycle of sMMO.

High-spin (S = 2) oxoiron(IV) is postulated as an active species in nonheme oxygenases,[14] and some high-spin (S =2) oxoiron(IV) complexes have been reported as model compounds.[15] Most of them, however, are less reactive to external substrate due to the steric hindrance of the ligands, except for the high reactivity of a high-spin oxodiiron(III)(IV) mixed valence complex with a tpa-type mononucleating ligand reported by Que et al.[16] Catalytic activity of the high-spin oxodiiron(III)(IV), however, has not been shown. Therefore, 6-hpa is only one ligand, known so far, capable of attaining not only the reversible O-O bond scission of peroxodiiron(III) to high spin oxodiiron(IV) but also the efficient catalysis of the epoxidation of various alkenes.

A similar dinucleating ligand where the pyridyl groups of 6-hpa are substituted with the carboxylate groups may be useful for examining the roles of carboxylate-rich coordination environment of O_2-activating non-heme diiron enzymes. So, we synthesized a

new carboxylate-containing dinucleating ligand, 1,2-bis[2-(*N*-2-pyrid-ylmethyl-*N*-glycinylmethyl)-6-pyridyl]ethane (H_2BPG_2E) (see Scheme 1(B)). In the H_2BPG_2E ligand, two tetradentate *N,N*-bis(2-pyridylmethyl)glycine (BPG) moieties are connected by a structurally flexible -CH_2CH_2- tether at the 6-positions of pyidyl groups. The -CH_2CH_2- tether is common in 6-hpa and H_2BPG_2E, but two pyridyl groups are substituted with two carboxyl groups in H_2BPG_2E. H_2BPG_2E forms μ-oxodiaquadiiron(III) complexes $[Fe_2(\mu\text{-}O)(H_2O)_2(BPG_2E)]X_2$ [X = ClO_4 (**2a**) or OTf (**2b**)] that efficiently catalyzes epoxidation of various alkenes with H_2O_2. Upon reaction of **2b** with H_2O_2, a new purple species was formed and isolated at low temperatures. The purple species was characterized spectroscopically. Here, we report the synthesis, crystal structures, and H_2O_2 activation of diiron complexes with BPG_2E. The roles of the carboxylate donor in the O-O bond scission will be discussed in comparison of the BPG_2E complexes with the corresponding 6-hpa complexes.

Scheme 1. Chemical structures of (A) 6-hpa and (B) H_2BPG_2E

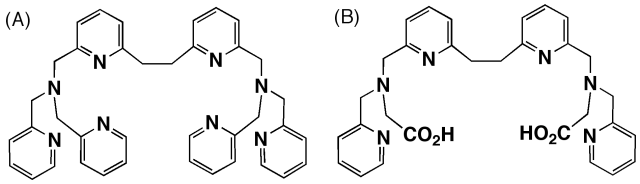

Results and discussion

The BPG_2E ligand specifically stabilizes μ-oxodiiron(III) core in a solution as shown by the ESI MS spectrum of **2b** where the parent peak due to $\{[Fe_2O(BPG_2E)]OTf\}^+$ appears at *m/z* 815 as a major one (Figure S6). The crystal structures of **2a** and **2b** have been determined by X-ray analysis with high-resolution quality (see Experimental section and Supporting Information), where a μ-oxodiaquadiiron(III) core is encapsulated by BPG_2E as shown in the ORTEP view of **2a** (Figure 1). The ORTEP view of **2b** is almost identical with that of **2a** (Figure S5). The Fe(III) ions adopt distorted octahedral geometry. The diaqua moiety is in a syn-binding mode with the average Fe-O_{aq} bond distances 2.064 and 2.056 Å and the O_{aq}•••O_{aq} distances 4.025 and 3.926 Å for **2a** and **2b**, respectively. These distances are slightly different between **2a** and **2b** due to the different hydrogen bonding structures of the diaqua ligands (see Figure S1 and S3). The syn-binding mode of the diaqua moiety is common in all μ-oxodiaquadiiron(III) complexes with various carboxylate-containing ligands reported so far.[12,17] Contrarily, with tpa-type polypyridine ligands, diaqua moiety generally adopts an anti-binding mode in μ-oxodiaquadiiron(III) complexes, including **1**.[13a] Since the pyridyl (py) group is larger than aqua, two aqua/py pairs occupy syn-positions of μ-oxodiaquadiiron core in **1** to prevent steric repulsion between py groups, leading to the anti-diaqua binding mode. Meanwhile, carboxylate/py pairs can occupy syn-positions of μ-oxodiaquadiiron core in **2a** and **2b** since carboxylate group is less sterically hindered than py, resulting in the syn-diaqua binding mode. Thus, the size of the pendant carboxyl and py groups seems to fix the binding mode of the diaqua moiety. The size of pendant groups may decisively affect the stability of peroxo complexes of BPG_2E and 6-hpa to control the O-O bond scission.

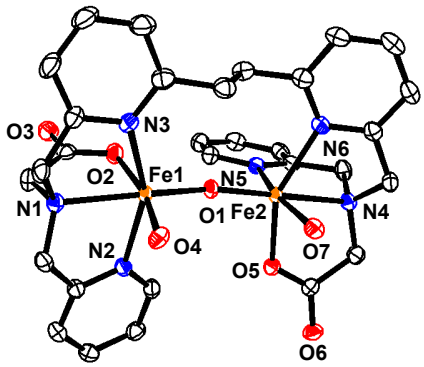

Figure 1. ORTEP view (70% probability) of the cationic portion of **2a**. Selected bond distances [Å] and angle [°]: Fe1···Fe2 3.568, Fe1-O1 1.7869(13), Fe1-O2 2.0217(12), Fe1-O4 2.0657(14), Fe1-N1 2.2632(16), Fe1-N2 2.1471(13), Fe1-N3 2.1833(12), Fe2-O1 1.7932(13), Fe2-O5 2.0105(10), Fe2-O7 2.0619(12), Fe2-N4 2.2656(16), Fe2-N5 2.1291(15), Fe2-N6 2.1837(14); Fe1-O1-Fe2 170.43(6).

2b catalyzed the epoxidation of alkenes with H_2O_2 in the presence of Et_3N (2 eq) in MeCN, where *trans*-β-methylstyrene was converted to the epoxide in 99% yield based on H_2O_2 used. The turnover number of **2b** exceeded 120. **2b** showed catalase activity at temperatures higher than 0°C, and both the yield of epoxide and the turnover number were reduced upon addition of H_2O. Therefore, H_2O_2 was slowly added using syringe pump to keep the concentration of free H_2O_2 low in the catalytic reaction. The detailed reaction conditions are described in Experimental section. It is noted that 1,2-*cis*-diol, often produced in the alkene oxidation catalyzed by monoiron complexes with H_2O_2, was not detected at all in the reaction of **2b**. When *cis*-β-methylstyrene and *cis*-cyclooctene were used as substrates, the yields of the epoxide were 43 and 15% based on H_2O_2 used, respectively, and for the former substrate, *cis*- and *trans*-epoxides were produced in 6 and 37% yield, respectively. Moreover, when the reaction using *trans*- and *cis*-β-methylstyrene as a substrate was carried out under O_2-atmosphere benzaldehyde was produced in the yield of 98 and 40 % based on the H_2O_2 used, respectively (see Table S11). These results suggested that a cation-radical intermediate was formed via one-electron oxidation of alkene. The cation radical may undergo the configuration change to form *trans*-epoxide from *cis*-alkene in the subsequent reactions, while under O_2 atmosphere it may afford benzaldehyde as a multi-electron oxidation product. On the basis of these results it is expected that an active species capable of oxidizing the alkene is formed upon reaction of **2b** with H_2O_2. Therefore, **2b** can be a promising functional sMMO model to study roles of the carboxylate donor in the dioxygen activation and substrate oxidation. However, it took ten-fold longer time to add H_2O_2 in the epoxidation catalyzed by **2b** than by **1**. This is due to the catalase activity and a very slow H_2O_2 activation by **2b**.

To detect the intermediates in the activation of H_2O_2, we carried out spectral pursuit for the reaction of **2b** with H_2O_2. Upon addition of an excess amount of H_2O_2 to **2b** in the presence of Et_3N (3 eq) in MeCN/H_2O (10:1, v/v) at -10°C, a dark purple species **3** was generated, and showed absorption bands at 452 nm (ε = 1420 $M^{-1}cm^{-1}$), 546 (1300), and 700 (300) (see Figure 2). These data are similar to 462 nm (ε = 1100 $M^{-1}cm^{-1}$), 577 (1500), and 750 (200) of $[Fe_2(\mu\text{-}O)(\mu\text{-}O_2)(6\text{-}Me_2\text{-}BPP)_2]$,[11] suggesting that **3** has a similar μ-oxo-μ-peroxodiiron(III) core.

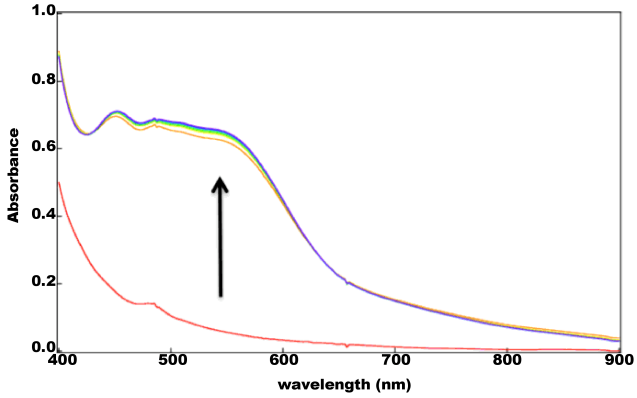

Figure 2. Electronic absorption spectral change in the formation of the intermediate **3** upon addition of 3 equiv of Et_3N and 100 equiv of H_2O_2 to **2b** (0.5 mM) in MeCN/H_2O (10:1, v/v) at -10ºC under N_2. Each spectrum is recorded at 5-second interval.

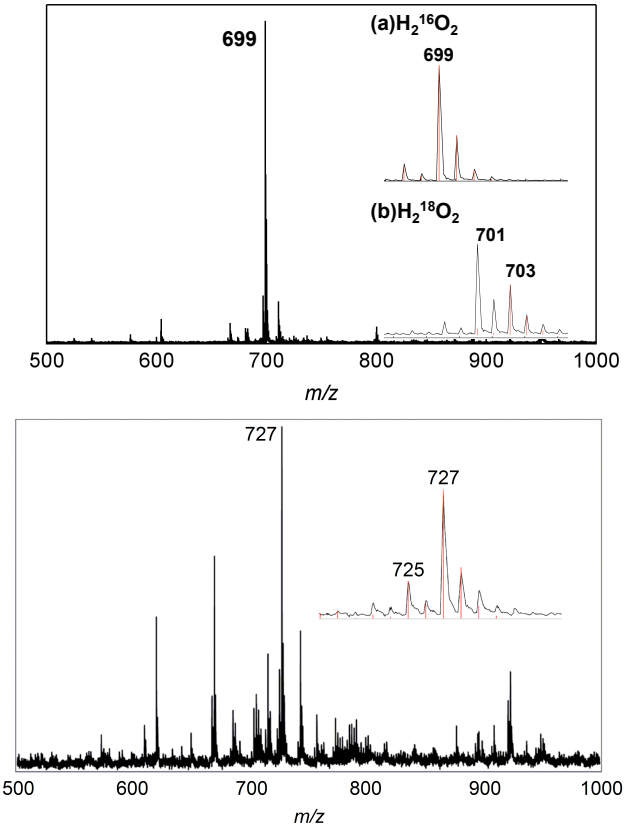

Figure 3. Upper: cold-spray ionization (CSI) MS spectra of **3** in MeCN/H_2O (10:1, v/v) showed a major peak at *m/z* 699 corresponding to $\{H[Fe_2O_3(BPG_2E)]\}^+$. The isotope patterns of the major peak observed with (a) $H_2{}^{16}O_2$ and (b) $H_2{}^{18}O_2$ are shown in the insets. The red lines are theoretical isotope patterns. Lower: CSI MS spectra of $^{18}O_3$-**3** obtained upon reaction of ^{18}O-**2b** with $H_2{}^{18}O_2$ in MeCN/$H_2{}^{18}O$ (10:1, v/v) showed a major peak at *m/z* 727 corresponding to $\{Na[Fe_2O_3(BPG_2E)]\}^+$. The isotope pattern of the major peak with theoretical red lines calculated for a 18 : 82 mixture of $^{18}O_2$-labeled **3** and $^{18}O_3$-labeled **3** is shown.

Cold-spray ionization (CSI) MS spectrum of **3** generated as shown above in MeCN/H_2O (10:1, v/v) shows a strong major peak at *m/z* 699, corresponding to $\{H[Fe_2O_3(BPG_2E)]\}^+$ as shown in Figure 3 upper. When **3** was ^{18}O-labeled with $H_2{}^{18}O_2$, the major peak was shifted to *m/z* 701 and 703 (see Figure 3 upper). The shift by four mass units demonstrated that two ^{18}O-atoms were incorporated into **3** from $H_2{}^{18}O_2$, suggesting the existence of a peroxo moiety in **3**. This is consistent with the presence of a μ-oxo-μ-peroxodiiron(III) core in **3** suggested by the electronic spectrum. Meanwhile, the two mass unit shift may be reasonably explained if the peroxo moiety of **3** undergoes O-O bond scission under the CSI MS conditions to generate μ-oxodioxodiiron(IV) **4**, and one of the terminal O-atoms of the O=Fe(IV)-O-Fe(IV)=O moiety is exchanged with H_2O. Moreover, ^{18}O-labeled **2b** was prepared from **2b** in MeCN/$H_2{}^{18}O$ (10:1, v/v) as shown in Experimental section, and 86% of ^{18}O-incorporation into the μ-oxo O-atom is estimated from the intensity ratio of the isotope peaks as shown in Figure S7. Fully labeled $^{18}O_3$-**3** was prepared upon addition of 50 eq. of $H_2{}^{18}O_2$ in MeCN to a solution of ^{18}O-labeled **2b** in the presence of 3 eq. of Et_3N in MeCN/$H_2{}^{18}O$ (10:1, v/v) at -10°C. The $H_2{}^{18}O_2$ in MeCN was contaminated by a small amount of $H_2{}^{16}O$, which was less than 10% of $H_2{}^{18}O$ used. The CSI MS spectrum of fully labeled $^{18}O_3$-**3** shows major peak corresponding to $\{Na[Fe_2O_3(BPG_2E)]\}^+$ with the isotope peaks at *m/z* 721, 723, 725, and 727 in the intensity ratio of 1 : 7 : 21 : 71, respectively (see Figure 3 lower). The fact that the major isotope peak appeared at 727, shifted by six mass units from 721, clearly showed that three O-atoms of μ-oxo and μ-peroxo in **3** were ^{18}O-labeled. The ratio between $^{18}O_2$-**3** and $^{18}O_3$-**3** estimated from the intensity of isotope peaks is 18 : 82, close to the 14 : 86, ratio between **2b** and ^{18}O-labeled **2b**. The slight difference may be due to the exchange of the terminal O-atoms of ^{18}O=Fe(IV)-^{18}O-Fe(IV)=^{18}O of **4** with $H_2{}^{16}O$. However, such O-atom exchange was not observed in the corresponding 6-hpa complexes.[13b] Thus, the carboxylate donor of BPG_2E strongly affects the reactivity of the Fe(IV)=O. The anionic character of the carboxylate donor may decrease the Lewis acidity of the Fe(IV) to make release of the terminal O-atoms easier. This may promote the exchange of the terminal O-atoms with H_2O. As a similar effect, it has been reported that the carboxylate donor weakens the Fe-O_{peroxo} bond in $[Fe_2(\mu\text{-}O)(\mu\text{-}O_2)(6\text{-}Me_2\text{-}BPP)_2]$.[11,18]

Upon addition of an excess amount of cold Et_2O to a solution of **3** generated as shown above, **3** was isolated as solid, and the isolated yield was 60% based on **2b** used. The elemental analysis of **3** agreed well with a formula $[Fe_2O_3(BPG_2E)]\bullet 8H_2O$. On the basis of the elemental analysis and spectral data, **3** is consistent with its assignment as μ-oxo-μ-peroxodiiron(III) $[Fe_2(\mu\text{-}O)(\mu\text{-}O_2)(BPG_2E)]$, and based on alkene epoxidation and O-atom exchange upon ^{18}O-labelling in the CSI MS measurements, it is suggested that **3** is converted to μ-oxodioxodiiron(IV) $[Fe_2(\mu\text{-}O)(O)_2(BPG_2E)]$ (**4**) via O-O bond scission. As shown below, the conversion of **3** to **4** is observed by Mössbauer and IR spectral measurements using the isolated solid. The presumed transformation of **2** to **3** and **4** is shown in Scheme 2.

Scheme 2. Transformation of **2** to μ-oxo-μ-peroxodiiron(III) **3** and μ-oxodioxodiiron(IV) **4**.

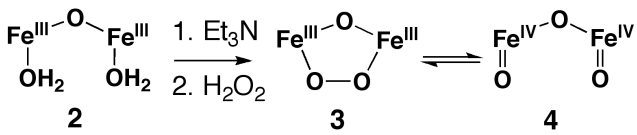

The zero-field Mössbauer spectra of the isolated dark purple

species were recorded at some different temperatures raised from 23 to 295 K, then recorded again using the same sample by recooling to 17 K as shown in Figure 4. The spectrum at 23 K mainly consists of two quadrupole doublets with δ = 0.481(2) mm/s, ΔE_Q = 1.657(2) mm/s and δ = 0.20(3), ΔE_Q = 0.40(6), as shown by the deconvolution spectra composed of components ***a*** (red spectrum) and ***b*** (blue spectrum) in Figure 4(A), respectively. The intensity ratio of ***a*** and ***b*** is almost 90 : 10 at 23 K. When the temperature was increased to 100, 200, 250, and 293 K the component ***a*** (red spectrum) was decreased with the increase of ***b*** (blue spectrum) as shown in Figure 4(B)-(E). The ratios of ***a*** : ***b*** estimated from the deconvolution spectra are 85 : 15, 76 : 24, 59 : 41, and 45 : 55 at 100, 200, 250, and 293 K, respectively. The δ and ΔE_Q values of ***a*** at 100 K, 0.392(4) and 1.650(2) mm/s, are close to 0.50 and 1.46 mm/s of μ-oxo-μ-peroxodiiron(III) [Fe_2(μ-O)(μ-O_2)(6-Me_2-BPP)$_2$] at 80 K,[11] and to 0.53-0.68 and 1.51-1.90 mm/s of peroxodiiron(III) intermediate P in sMMO[2] and their model compounds.[19] Thus, component ***a*** may be assigned to μ-oxo-μ-peroxodiiron(III) **3** with a symmetric structure. These values, however, are largely different from Mössbauer parameters δ and ΔE_Q = 0.54 and 0.58 mm/s for a peroxodiiron(III) form of ToMOH,[7] and 0.66 and 0.58 mm/s for a peroxo complex generated from [Fe_2(μ-O)(H_2O)$_2$(BPG_2DEV)](ClO_4)$_2$.[12] The δ and ΔE_Q values of the component ***b*** at 24-293 K, 0.131(3)-0.26(2) and 0.40(6)-0.55(3) mm/s, are almost in the range of δ = 0.14-0.21 and ΔE_Q = 0.53-0.68 mm/s of high-spin oxodiiron(IV) in the intermediate Q of sMMO.[2,20] High-spin (*S* = 2) oxoiron(IV) complexes reported so far show the δ and ΔE_Q values around 0.1 and 0.5 mm/s, respectively,[15] but low-spin (*S* = 1) oxoiron(IV) complexes have relatively higher ΔE_Q values of 1-2 mm/s.[21] Thus, component ***b*** may be assigned to high-spin oxodiiron(IV) similar to the intermediate Q and the synthetic high-spin oxoiron(IV) complexes. The Mössbauer spectra of starting material **2b** and decomposed product of **3** at 77 K show quadrupole doublets with δ = 0.461(2) mm/s, ΔE_Q = 1.670(2) mm/s and δ = 0.453(2) mm/s, ΔE_Q = 1.664(2) mm/s, respectively (Figure S8). Since these data are temperature-independent and clearly different from δ = 0.24(2) mm/s, ΔE_Q = 0.48(4) mm/s of the component ***b*** at 50 K, the components ***a*** and ***b*** can be distinguished from the starting material and decomposed product. In conjunction with the elemental analysis and the electronic absorption and CSI MS spectra, conclusively, the components ***a*** and ***b*** are assigned to μ-oxo-μ-peroxodiiron(III) **3** and high-spin μ-oxodioxodiiron(IV) **4**, shown in Scheme 2, respectively.

Moreover, when the Mössbauer spectrum was recorded upon recooling the same sample to 17 K the increase of component ***a*** and the concomitant decrease of component ***b*** were observed, where the ratio of ***a*** and ***b*** is 82 : 18 with a small amount, 7%, of a quadrupole doublet assignable to diiron(II) as shown in Figure 4(F). The spectrum thus obtained is completely equal to that obtained by the first measurement at 23 K. Thus, the temperature-dependent Mössbauer measurements clearly showed that **3** and **4** are interconverted each other. To the best of our knowledge, this is the first example of reversible conversion of peroxodiiron(III) to high-spin oxodiiron(IV) with a carboxylate-containing ligand. This reversibility is attained because of the bistability of **3** and **4**. The flexible -CH_2CH_2- tether in the BPG_2E ligand may enable the bistability of peroxodiiron(III) and high spin oxodiiron(IV) states as it was observed in the reversible O-O bond scission of the corresponding diiron complexes with a 6-hpa ligand.[13b]

On the basis of the Mössbauer data in this work and those reported for the diiron complexes with 6-hpa, the ratios of the peroxodiiron(III) to the oxodiiron(IV) at 295 K are 45 : 55 and 15 : 85 for the BPG_2E and the 6-hpa complexes,[13b] respectively. These data show that BPG_2E relatively stabilizes the peroxo state rather than the oxodiiron(IV) state as compared with 6-hpa. This may be explained by the structural effect of the pendant carboxylate and pyridyl groups shown in the crystal structures of **2a** and **1**, where BPG_2E stabilizes a syn-binding mode, and 6-hpa does an anti-binding mode. Since it is rational that the peroxo moiety of **3** takes a syn-like binding mode similar to that of [Fe_2(μ-O)(μ-O_2)(6-Me_2-BPP)$_2$],[11] BPG_2E may stabilize the syn-type structure of the Fe-O-O-Fe moiety in **3**. Conversely, it turns out that 6-hpa destabilizes the syn-like binding mode of Fe-O-O-Fe moiety to promote the O-O bond scission. This suggests that the O-O bond scission of peroxodiiron(III) to oxodiiron(IV) can be controlled by the size of the pendant groups.

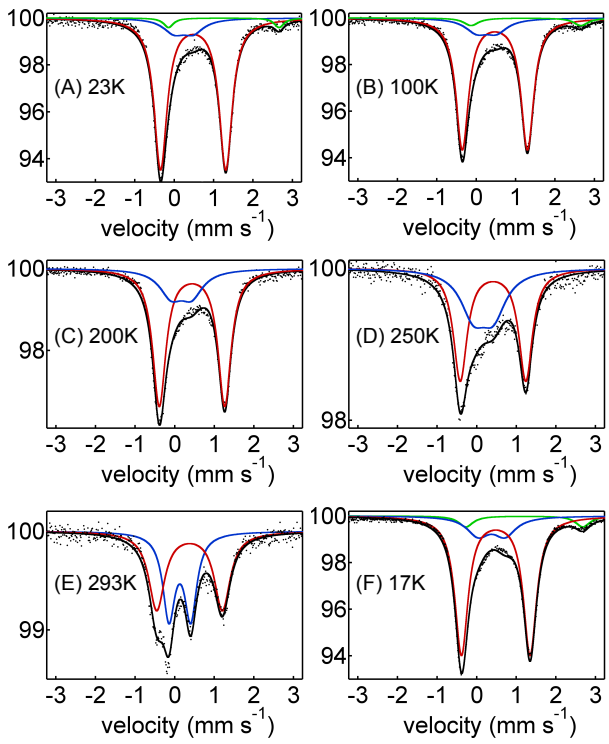

Figure 4. Zero field Mössbauer spectra of the isolated solid, recorded by raising the temperatures at (A) 23, (B) 100, (C) 200, (D) 250, and (E) 293 K, and by recooling the same sample at (F) 17 K. The black line is the least-square fitting to the raw data, and the red (component ***a***), blue (component ***b***), and green (component ***c***) lines are the deconvolution spectra corresponding to μ-oxo-μ-peroxodiiron(III) **3**, μ-oxodioxodiiron(IV) **4**, and diiron(II) complexes.

The peroxo moiety of the μ-oxo-μ-peroxodiiron(III) **3** was detected by resonance Raman (RR) measurements. To examine the origin of the peroxo O-O atoms in **3** four different experiments were carried out where **2b** and ^{18}O-labeled **2b** were used for the reaction with $H_2{}^{16}O_2$ and $H_2{}^{18}O_2$ in aqueous MeCN at -30°C. The ^{18}O-labeled **2b** was prepared by treating **2b** with an excess amount of $H_2{}^{18}O$ in MeCN under N_2 at 70°C. The incorporation of one ^{18}O-atom was monitored by the ESI MS spectra, and 86% of **2b** was converted to ^{18}O-labeled **2b** in 30 min (see Figure S7). The RR spectra obtained with 607 nm excitation for four different samples prepared with (a) **2b**/$H_2{}^{16}O_2$,

(b) ^{18}O-labeled **2b**/$H_2{}^{16}O_2$, (c) **2b**/$H_2{}^{18}O_2$ and (d) ^{18}O-labeled **2b**/$H_2{}^{18}O_2$ are shown in Figure 5(a)-(d), respectively. The spectra of (a) and (b) show a clear band at 835 cm^{-1} (Figure 5(a), (b)). This band is in the range of 822-919 cm^{-1} reported as O-O stretching vibration of peroxodiiron(III) complexes.[22] The band shifted to 784 cm^{-1} by ^{18}O-labelling with $H_2{}^{18}O_2$ as shown in the spectra of (c) and (d) (Figure 5(c), (d)). The observed isotope shift by 51 cm^{-1} is close to 48 cm^{-1} expected based on a harmonic O-O oscillator model, but much larger than 37 cm^{-1} expected for a stretching vibration of the terminal Fe(IV)=O. Thus, the band at 835 cm^{-1} is assigned to the O-O stretching vibration of the μ-oxo-μ-peroxodiiron(III) **3**, and the O-O moiety comes from hydrogen peroxide but not from the coordinated H_2O molecules. It was reported that the stretching vibration of a terminal Fe(IV)=O in Fe(III)-O-Fe(IV)=O is shifted by ^{18}O-labeling of the μ-oxo bridge as shown by the bands at 840, 835, 797, and 794 cm^{-1} for Fe(III)-^{16}O-Fe(IV)=^{16}O, Fe(III)-^{18}O-Fe(IV)=^{16}O, Fe(III)-^{16}O-Fe(IV)=^{18}O, and Fe(III)-^{18}O-Fe(IV)=^{18}O, respectively.[23] If the band at 835 cm^{-1} comes from the Fe(IV)=O it must be affected by the ^{18}O-μ-oxo labeling. As shown in Figure 5, however, it was not changed at all by the ^{18}O-μ-oxo labeling. Therefore, the band at 835 cm^{-1} finally is assigned to the O-O stretching vibration of **3**, and apparently, the Fe(IV)=O of **4** is not detected in the RR spectra. Unfortunately, the RR band of the stretching vibration of Fe-O_{peroxo} bond in the peroxodiiron moiety of **3** was not obtained with 407 and 607 nm excitations.

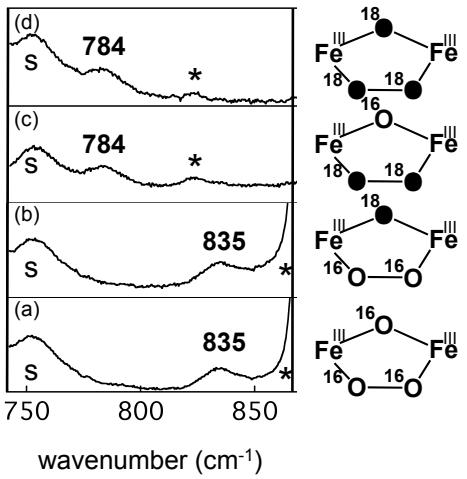

Figure 5. Resonance Raman spectra of **3** in MeCN at -30ºC obtained with excitation at 607 nm. The samples were prepared by treating **2b** or ^{18}O-labeled **2b** with 500 equiv of $H_2{}^{16}O_2$ or $H_2{}^{18}O_2$ ((a) **2b**/$H_2{}^{16}O_2$, (b) ^{18}O-labeled **2b**/$H_2{}^{16}O_2$, (c) **2b**/$H_2{}^{18}O_2$, and (d) ^{18}O-labeled **2b**/$H_2{}^{18}O_2$) in the presence of 2 equiv of Et_3N. The numbers shown in the spectra are the corresponding vibration bands of **3**. S and * means the solvent band and H_2O_2, respectively.

Finally, we observed a stretching vibration band of Fe(IV)=O in **4** at 810 cm^{-1}, using the isolated solid on the IR spectra at room temperature. The band was decreased with the decomposition of **4**. This may take place upon reaction with H_2O_2 included as an impurity in the isolated solid due to the high catalase activity of **4**, and the rate seems to depend on the amount of H_2O_2 included. After thorough evacuation of H_2O_2 from the isolated solid under highly reduced pressure less than 10^{-5} Torr for more than three weeks at -40°C, the isolated solid gave the clear band at 810 cm^{-1}, which was kept intact for several minutes and gradually decreased over an hour as followed by the IR spectral change (Figure 6A/B). When **4** was labelled with $H_2{}^{18}O_2$, the band at 810 cm^{-1} disappeared and a band appeared at 774 cm^{-1} (Figure 6C), which decreased with time. The observed isotope shift 36 cm^{-1} is equal to the theoretical value 36 cm^{-1}, estimated based on a harmonic Fe-O oscillator model.[13b] Thus, conversion of **3** to **4** via O-O bond scission is shown by the IR as well as the Mössbauer measurements. The value 810 cm^{-1} is in a range of 798-842 cm^{-1} reported for Fe(IV)=O, and slightly weaker than 820 cm^{-1} observed by the RR spectra of μ-oxodioxodiiron(IV) complex with a 6-hpa ligand. This is a clear electronic effect of the carboxylate donor of BPG_2E that relatively decreases the Lewis acidity of Fe(IV) as compared with the pyridine donor of 6-hpa. This is consistent with the easy O-atom exchange of Fe(IV)=O in **4** described above in the CSI MS measurements.

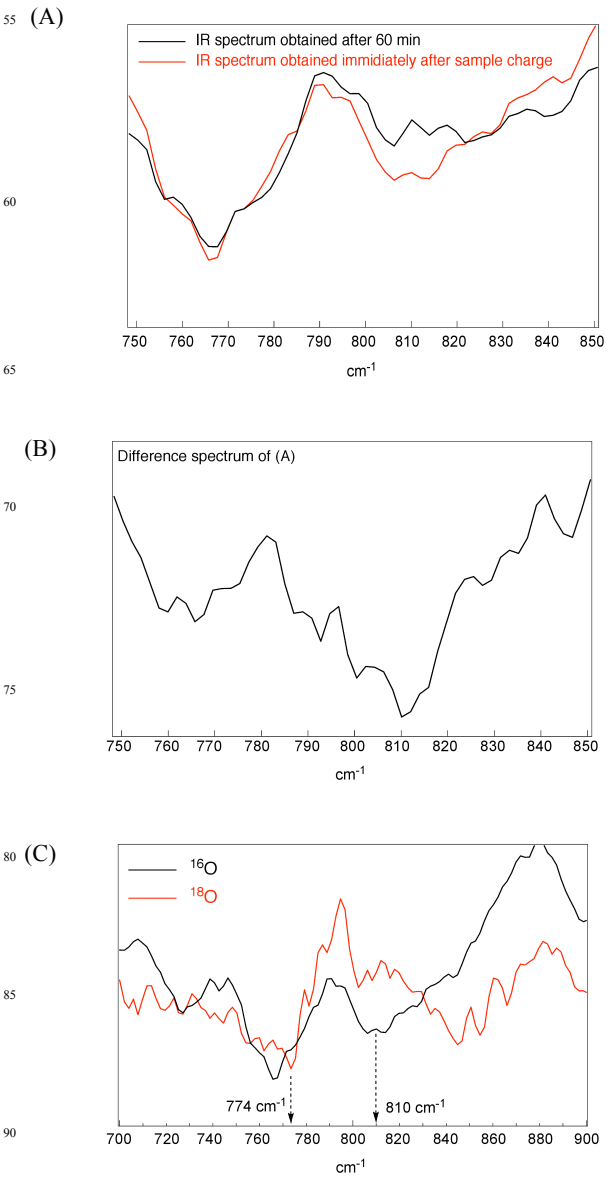

Figure 6. IR spectra of the isolated solid recorded at room temperature; (A) red: immediately after sample charge, black: 60 min later, (B) difference spectrum of (A), (C) red: ^{18}O-labelled, black: non-labelled.

Decomposition of **3**, prepared with **2b** (5.0×10^{-4} M) and H_2O_2 (1.2 eq) in the presence of Et_3N in MeCN/H_2O (10:1, v/v), was monitored at 546 nm, and obeyed first-order kinetics with $k = 1.5 \times 10^{-3}$ s^{-1} at -10°C as shown in Figure 7. Upon addition of *trans*-β-methylstyrene as a substrate in the concentration range of 2.5×10^{-2} to 1.0×10^{-1} M, the decay rate was not accelerated at all as shown in Figure 8. These results demonstrated that **3** is not the direct oxidant, and accordingly it is likely that the O-O bond scission of **3** to **4** is the rate-determining step. Therefore, it is difficult to accumulate **4** in a solution. This is consistent with the fact that the Fe(IV)=O of **4** could not be detected in a solution by the RR spectra. We carried out Arrhenius plot for the thermal decomposition of **3** to estimate the activation energy ΔE_a (see Experimental section for the details of the kinetic studies and the plot in Figure S9). The observed ΔE_a value is 22.8 kcal/mol, close to 21.9 kcal/mol estimated by DFT calculation vide infra (Figure 9).

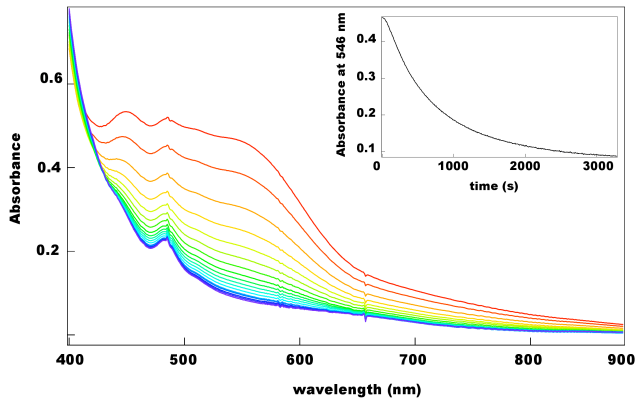

Figure 7. Electronic absorption spectral change upon decomposition of **3** (5.0×10^{-4} M) in MeCN/H_2O (10:1, v/v) at -10°C (insert: time trace of absorbance at 546 nm).

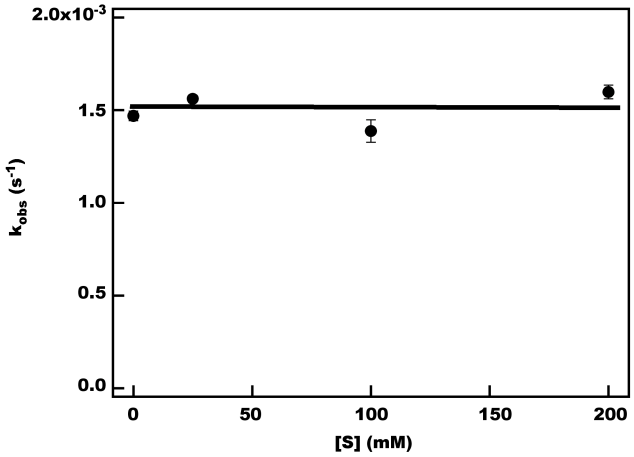

Figure 8. Plot of k_{obs} vs [S], the substrate concentration, in the reaction of **3** (0.5 mM) with *trans*-β-methylstyrene (with 0 eq., 50 eq., 200 eq., 400 eq.) in MeCN/H_2O (10:1, v/v) at -10°C.

The O-O bond scission of **3** to **4** is the rate-determining step, but was detected by the isotope-labeling experiments in the CSI MS measurements as an exchange of the O-atom of Fe(IV)=O with H_2O as shown above. The mass spectrometric conditions are unusual in that high electric potential is charged to ionize sample. Under such conditions, the O-O bond scission may be accelerated to give **4**, which may have a lifetime necessary to be detected. The reason may be because **4** is isolated from H_2O_2 in gaseous atmosphere under the CSI MS conditions. When using the isolated solid thoroughly dried, the reversible conversion of **3** to **4** was shown by the temperature-dependent Mössbauer spectra, and the stretching vibration band of Fe(IV)=O in **4** was detected in the IR spectra. These results commonly indicate that **4** can be detected spectroscopically when it is free from H_2O_2.

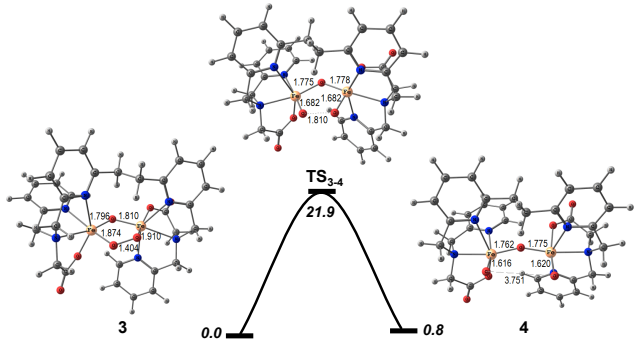

Figure 9. Calculated energy diagram for the O-O bond scission of **3** to **4**. Selected bond distances in Å are given along with the relative energies in kcal/mol.

To rationalize the mechanism of the reversible conversion of **3** to **4** as proposed in Scheme 2 as well as to corroborate the temperature dependence of the Mössbauer spectra, we carried out DFT calculations. In the optimized diiron structures of **3** and **4** in Figure 9, the Fe centers are in octahedral environments in which the Fe-Fe distances are 3.093 and 3.466 Å, respectively. Calculated spin densities at the two Fe centers are (4.11 and -4.14), and (3.25 and -3.20) respectively for complexes **3** and **4**, due to the antiferromagnetic spin coupling at the Fe centers. In complex **3** the O_2 displays a bridging bond in a μ-η^1:η^1-O_2 fashion with a O-O distance of 1.404 Å whereas in **4** the O-O distance is 3.751 Å, indicating that the O-O bonding interaction is absent in the μ-oxodioxodiiron(IV) complex. The computed energy diagram for the O-O bond scission of **3** to **4** at 298 K is depicted in Figure 9. The reaction via transition state $\mathbf{TS_{3-4}}$ is slightly endothermic by 0.8 kcal/mol with an activation barrier of 21.9 kcal/mol. In this transition state the O-O distance is elongated by 0.406 Å. As it is evident from the Mössbauer spectra, the O-O bond cleavage of **3** occurs at relatively high temperature because of the larger activation barrier needed for this process and the maximum population of **4** is observed at the highest temperature 293K. The recooling of the sample **4** from 295 K leads the rebinding of the oxygen atoms and hence complex **3** is thermodynamically and kinetically obtained. Thus, the DFT studies nicely support the experimental findings of the reversible O-O bond scission.

Although in a solution, **4** can not be detected at all because O-O bond scission of **3** is the rate-determining step, O-O bond scission smoothly proceeds for the peroxo complex with 6-hpa ligand as previously reported.[13b] Moreover, it took ten-fold longer time for addition of H_2O_2 by syringe-pump to gain good yield for the epoxidation catalyzed by **2b** than that by **1**.[13a] This may be caused by both the slower O-O bond scission of **3** and the higher catalase activity of **4**. The BPG_2E ligand may stabilize the syn-binding mode of **3** and **4** to retard the O-O bond scission of **3** and to enhance the catalase activity of **4** leading to the non-productive decomposition. As described for the crystal structures of **2a** and

2b, the syn-binding mode is caused by the sterically less hindered pendant carboxylate group of BPG_2E. Therefore, it is suggested that the O-O bond scission of the peroxo species and the catalase activity of μ-oxodioxodiiron(IV) species are strongly affected by the size of the pendant groups to determine the overall rate of the catalytic reaction.

The importance of the size of the carboxylate donor has been pointed out for the first time in comparison between BPG_2E and 6-hpa in this study. In the biological relevance, it is suggested that the carboxylate donor may play an important role in the stability of peroxo intermediates in the catalytic cycles of sMMO, TMO, ToMO and DOHH. Since a carboxylate donor is sterically less hindered, there is no steric repulsion between the donor groups located at the syn-position, and the Fe-O-O-Fe of peroxo intermediate can easily take the most stable structure. This may lead to the high thermal stability of the peroxo intermediate as in DOHH. The stability of the peroxo intermediate can be controlled by the conformation change, where it may bring about the change of the syn-binding mode to the anti-binding mode to facilitate the O-O bond scission. This aspect may give a new insight into the roles of the carboxylate donors in the dioxygen activation of the non-heme diiron enzymes.

Conclusions

A carboxylate-containing dinucleating ligand H_2BPG_2E and its μ-oxodiaquadiiron(III) complexes $[Fe_2(\mu\text{-}O)(H_2O)_2(BPG_2E)]X_2$ (X = ClO_4 (**2a**) and TfO (**2b**)) were synthesized to mimic diiron centers surrounded by a common carboxylate-rich coordination environment of the O_2-activating non-heme diiron enzymes. **2b** efficiently catalyzed the epoxidation of various alkenes with H_2O_2. A dark purple species was formed as an intermediate upon reaction of **2b** with H_2O_2, and isolated upon addition of an excess amount of cold Et_2O. The purple species was assigned to the μ-oxo-μ-peroxodiiron(III) $[Fe^{III}_2(\mu\text{-}O)(\mu\text{-}O_2)(BPG_2E)]$ (**3**) on the basis of the electronic absorption, CSI MS, and RR spectra. Moreover, on the basis of Mössbauer and IR spectra obtained by using the isolated solid, it was shown that **3** was converted to the high-spin μ-oxodioxodiiron(IV) $[Fe^{IV}_2(\mu\text{-}O)(O)_2(BPG_2E)]$ (**4**). The kinetic studies and the substrate oxidation showed that the active species is generated via the rate-determining O-O bond scission. This is the first example for the reversible O-O bond scission of peroxodiiron(III) to high spin oxodiiron(IV) with a carboxylate-containing ligand. Comparisons of the structures and reactivity of peroxo complexes with BPG_2E and 6-hpa clarified roles of the carboxylate donors in the O-O bond scission. With 6-hpa, the O-O bond scission of peroxodiiron(III) to high spin oxodiiron(IV) smoothly proceeded. On the contrary, BPG_2E stabilizes the peroxodiiron(III) to retard the O-O bond scission. This remarkable effect was reasonably explained by the size difference in the carboxylate and pyridine donors of BPG_2E and 6-hpa, respectively. Although the electronic effect of carboxylate donor has not been clarified for the O-O bond scission yet, it was shown that carboxylate donor of BPG_2E weakens the Fe(IV)=O bond on the basis of the 10 cm^{-1} low frequency shift of stretching vibration of Fe(IV)=O of **4** and easy exchange of the O-atom as compared with the pyridine donor of 6-hpa. This may suggest that in the non-heme diiron enzymes, similarly, the carboxylate donors may sterically stabilize the peroxodiiron(III) state, and therefore, the generation of high spin oxodiiron(IV) via the O-O bond scission may require a specific conformational change at the diiron center.

Experimental section

Materials

All ordinary reagents and solvents were purchased and used as received unless otherwise noted. MeCN was dried over P_2O_5 and distilled. Alkenes used in this study were purified by distillation and treatment with alumina column just before use. A solution of H_2O_2 in MeCN was prepared by concentration of 40% aqueous H_2O_2 and addition of MeCN, and determined by redox titration with $KMnO_4$. Et_3N was purified by distillation from sodium, and kept on NaOH. A solution of Et_3N in MeCN was determined by titration.

Measurements

Elemental analyses (C, H, and N) were carried out on a Perkin-Elmer Elemental Analyzer 2400 II. UV-vis absorption spectrum was recorded on an Agilent 8543 UV spectroscopy system with a Unisoku thermostated cell holder designed for low-temperature measurements. Cold spray ionization (CSI) mass spectra were obtained on a JEOL JMS-T100CS spectrometer in MeCN solution at low temperatures. GLC analysis was performed on a Shimadzu GC-2014 gas chromatography equipped with a GL Science InertCap capillary column (60 m × 0.25 mm). Infrared (IR) spectra were recorded on a SHIMADZU Single Reflection HATR IRAffinity-1 MIRacle 10. ^{1}H-NMR spectra were recorded on a JEOL ECA-500RX spectrometer using Me_4Si as an internal standard. Mössbauer spectra were measured at Nishina Center, The Institute for Physical and Chemical Research (RIKEN). The Mösbauer spectra of **2b** and the decomposed product of the peroxo complex were measured at Kyoto University Research Reactor Institute. The radioactive source was ^{57}Co(Rh). Isomer shifts were reported relative metallic iron foil. Resonance Raman (RR) scattering was excited at 407 and 607 nm using an Ar-dye-laser and detected with CCD detector (Princeton Instruments) attached to a single polychrometer. All measurements were at -30°C using a spinning cell. Raman shifts were calibrated with indene, and the accuracy of the peak positions of the Raman bands was ± 1 cm^{-1}.

Structure Determination of Single Crystals. The crystal structures of **2a** and **2b** were determined using a Rigaku R-AXIS RAPID diffractometer using multi-layer mirror monochromated Mo-Kα radiation. The data were collected at -180 ± 1°C to a maximum 2θ value of 54.9°. A total of 44 oscillation images were collected. A sweep of data was done using ω scans from 130.0 to 190.0° in 5.00° step, at χ=45.0° and ϕ = 0.0°. The exposure rate was 60.0 [sec./°]. A second sweep was performed using ω scans from 0.0 to 160.0° in 5.00° step, at χ=45.0° and ϕ = 180.0°. The exposure rate was 60.0 [sec./°]. The crystal-to-detector distance was 127.40 mm for **2a** and 127.00 mm for **2b**. Readout was performed in the 0.100 mm pixel mode. Of the 19147 and 20161 reflections were collected for **2a** and **2b**, where 8757 and 9218 were unique (R_{int} = 0.0180 and 0.0303); equivalent reflections were merged, respectively. An empirical absorption correction was applied which resulted in transmission factors ranging from 0.736 to 0.916 for **2a** and from 0.682 to 0.894 for **2b**. The data were corrected for Lorentz and polarization effects.

Crystal data for 2a•3H$_2$O. $C_{30}H_{40}Cl_2Fe_2N_6O_{18}$, triclinic, *P-1*, Z = 2, *a* = 11.4730(4), *b* = 12.9171(4), *c* = 14.4931(4) Å, α = 113.070(8)°, β = 100.094(7)°, γ = 90.982(6)°, *V* = 1936.75(17) Å^3, *μ*(MoKα) = 9.705 cm^{-1}, *Dc* = 1.638 g/cm^3, R_1 = 0.0281, wR_2 = 0.0757, for 8757 unique reflections, 599 variables, GOF = 1.060, CCDC reference number 978448

Crystal data for 2b•2H$_2$O. $C_{32}H_{38}F_6Fe_2N_6O_{15}S_2$, triclinic, *P-1*, Z = 2, *a* = 11.5827(3), *b* = 13.4954(3), *c* = 14.5372(3) Å, α = 114.729(8)°, β = 99.954(7)°, γ = 90.485(6)°, *V* = 2024.60(17) Å^3, μ(MoKα) = 9.227 cm^{-1}, *Dc* = 1.700 g/cm^3, R_1 = 0.0257, wR_2 = 0.0814, for 9218 unique reflections, 592 variables, GOF = 1.098, CCDC reference number 978449

Synthesis

1,2-bis[2-(2-pyridylmethyl)aminomethyl-6-pyridyl]ethane-*N,N′*-diacetic acid diethyl ester. A mixture of 1, 2-bis(6-bromomethyl-2-pyridyl)ethane·dihydrobromide 1.06 g (2.0 mmol), 2-pyridylmethyl glycine ethyl ester 0.777 g (4.0 mmol) and Na_2CO_3 2.12 g (20 mmol) in MeCN (15 ml) was stirred at room temperature for 24h. Then the glay precipitation was removed from the mixture. Water was added to the resulting solution and the solution was extracted with $CHCl_3$. The extracts were dried over Na_2SO_4 and evaporated. The crude product was isolated as red-brown oil and purified by alumina column chromatography (solvent: $CHCl_3$). The product was isolated as yellow oil (1.07 g, 90%). ^{1}H-NMR (Me$_4$Si,in CDCl$_3$): δ= 8.52 (*d*, 1H, py'-3), 7.65 (*t*, 1H, py'-4), 7.60 (*d*, 1H,py-5), 7.50 (*t*, 1H, py-4), 7.37 (*d*, 1H, py'-6), 7.14 (*t*, H, py'-5), 6.95 (*d*, 1H, py-3), 4.17(*q*, 2H, -C**H$_2$**CH$_3$), 3.99 (*s*, 2H, -C**H$_2$**N-), 3.96(*s*, 2H, -C**H$_2$**N-), 3.45 (*s*, 2H, -C**H$_2$**COO-), 3.17(*s*, 2H, -C**H$_2$C H$_2$**-), 1.25 ppm (*t*, 3H, -CH$_2$C**H$_3$**). ESI MS: *m/z* 619 [M+Na]$^+$.

2-bis[2-(2-pyridylmethyl)aminomethyl-6-pyridyl]ethane-*N,N′*-diacetic acid · nHCl (H$_2$BPG$_2$E·nHCl). To a mixture of THF (10 ml) and conc. HCl (1.5 ml) was added 1, 2-bis[2-(2-pyridylmethyl)aminomethyl-6-pyridyl]ethane-*N, N′*-diacetic acid diethyl ester 0.195 g (0.33 mmol). The mixture was stirred overnight at room temperature, and white solid precipitated. The white solid was collected by filtration, and washed with THF. The solid was excellent purity based on NMR without further purification (0.2 g, 89%). ^{1}H-NMR (Me$_4$Si,in D$_2$O): δ = 8.72 (*d*, 1H, py'-3), 8.52 (*t*, H, py'-5), 8.39 (*t*, 1H, py'-4), 8.03 (*d*, 1H, py'-6), 7.95 (*t*, 1H, py-4), 7.89 (*d*, 1H,py-5), 7.81 (*d*, 1H, py-3), 4.47 (*s*, 2H, -C**H$_2$**N-), 4.44 (*s*, 2H, -C**H$_2$**N-), 3.71 (*s*, 2H, -C**H$_2$**COO-), 3.57 ppm (*s*, 2H, -C**H$_2$C H$_2$**-). ESI MS: *m/z* 541 [M+H]$^+$, 563 [M+Na]$^+$.

[Fe$_2$(*μ*-O)(H$_2$O)$_2$(BPG$_2$E)](ClO$_4$)$_2$ (2a). An aqueous solution of NaOH was added to H$_2$BPG$_2$E · 4HCl 89 mg (0.13 mmol) in water to be adjusted to pH 5. The resulting solution was evaporated and dried in vacuo. The solid residue was dissolved in dry EtOH, and the insoluble solid was removed by filtration. The filtrate was evaporated. To the residue were added water and Fe(ClO$_4$)$_3$ · 7H$_2$O 125 mg (0.26 mmol). The pink-colored **2a** was precipitated and recrystallized from MeCN/ H$_2$O to give crystals suitable for X-ray structure analysis (47 mg, 40%). Elemental analysis of **2a**•3H$_2$O (%) calcd for $C_{30}H_{36}Cl_2Fe_2N_6O_{18}$: C 37.88, H 3.81, N 8.83; found: C 38.27, H 4.11, N 8.94. IR: ν = 1609, 1570 (pyridine ring), 1096 (ClO$_4$), 621 cm^{-1} (Fe-O-Fe). ESI MS: *m/z* 765 [M−2H$_2$O−ClO$_4$]$^+$.

[Fe$_2$(*μ*-O)(H$_2$O)$_2$(BPG$_2$E)](TfO)$_2$ (2b). An aqueous solution of NaOH was added to H$_2$BPG$_2$E · 4HCl 89 mg (0.13 mmol) in water to be adjusted to pH 5. The resulting solution was evaporated and dried in vacuo. The solid residue was dissolved in dry EtOH, and the insoluble solid was removed by filtration. The filtrate was evaporated, To the residue were added water and Fe(OTf)$_2$ · 2MeCN 113 mg (0.26 mmol). The mixture was stirred for 24h under O$_2$. The pink-colored **2b** was precipitated and recrystallized from MeCN/ H$_2$O to give crystals suitable for X-ray structure analysis (78 mg, 60%). Elemental analysis of **2b**•2H$_2$O (%) calcd for $C_{32}H_{34}F_6Fe_2N_6O_{15}S_2$: C 37.23, H 3.32, N 8.14; found: C 37.22, H 3.65, N 8.16. IR: ν = 1609, 1568 (pyridine ring), 631 cm^{-1} (Fe-O-Fe). ESI MS: *m/z* 815 [M−2H$_2$O−TfO]$^+$.

[Fe$_2$(*μ*-^{18}O)(H$_2$^{18}O)$_2$(BPG$_2$E)](TfO)$_2$ (^{18}O-labeled 2b). [Fe$_2$(*μ*-O)(H$_2$O)$_2$(BPG$_2$E)](TfO)$_2$ (**2b**) 30 mg (30 μmol) was dissolved in dry MeCN under N$_2$. ^{18}O-labeled water (H$_2$^{18}O) 200 μl (11 mmol) was added to the solution, and the solution was stirred at 70ºC. The reaction was monitored by the ESI MS spectra, and 86% of μ-oxo O-atom was labeled with ^{18}O-atom in 30 min (see Figure S7). The resulting solution was evaporated, and the pink-colored **^{18}O-labeled 2b** was obtained. ESI MS: *m/z* 817 [M−2H$_2$^{18}O−TfO]$^+$.

Preparation and isolation of 3. To a solution of **2b** (83.7 mg 83.7 μmol) in MeCN (1 mL) was added 2.0 equiv of Et$_3$N (120 mM) at -40°C. To the solution was added 500 equiv of H$_2$O$_2$ (10 M), and stirred for 5 min. The solution turned dark purple. To the solution was added 15 mL of Et$_2$O at -40°C, then purple solid precipitated. The supernatant was decanted off, and the precipitate was washed with Et$_2$O several times at -40 °C. The purple solid was dried in vacuo. The isolated solid is stable at low temperature, and not changed several days at room temperature under dark in the absence of organic compounds potentially acting as reductant. Yield 35.1 mg (60 %). Anal. Calcd for $C_{30}H_{46}N_6O_{15}Fe_2$: C, 42.77; H, 5.50; N, 9.98%. Found: C, 42.63; H, 4.90; N, 9.82%. The isolated solid was used for various spectral measurements including the Mössbauer spectra.

Reaction conditions for the epoxidation of alkenes

A solution of 1 mL of **2b** (1.0 × 10^{-3} M) in MeCN was placed in a flask equipped with a three-way cock, and quickly degassed by several cycles of evacuation and refilling with N$_2$ gas. To the solution were added a solution of Et$_3$N (2.0 equiv), 1 mmol of alkene, and 2 μl of nitrobenzene, then a solution of H$_2$O$_2$ (10 □mol) in MeCN (1.0 mL) was added over 5 h by using a syringe pump under N$_2$ atmosphere with stirring at 25°C. After further 30 min, a fraction of the solution was analyzed and assayed by GC. *cis*-Cyclooctene and *cis*-β-methylstyrene were also used as substrates instead of *trans*-β-methylstyrene, under the same reaction conditions. Moreover, different reaction conditions were examined as shown in Table S11.

General Procedures for Kinetic Studies

For the kinetic measurements, **3** was freshly prepared just before the kinetic measurements. A typical method used for the kinetic measurements was as follows. A solution of 2 mL of **2b** (5.0 × 10^{-4} M) in MeCN/H$_2$O (10:1, v/v) was placed in a quartz-cell equipped with a three-way cock, and quickly degassed by several cycles of evacuation and refilling with N$_2$ gas. The temperature was maintained at -10 ± 0.2°C during the measurements. To the solution were added a solution of Et$_3$N (3.0 equiv) in MeCN and after stirring for 2 min a solution of H$_2$O$_2$ (1.2 equiv) in MeCN. The spectral change was recorded in the range of 400-900 nm. The decrease of **3** was monitored at several different wavelengths. The first-order rate constants (k_{obs}) were obtained from fits of –ln(1-At/A$_\infty$) vs time. The spontaneous decomposition rate of **3** was obtained in the absence of a substrate as shown above. Here, *trans*-β-methylstyrene was used as a substrate, and the decomposition rate of **3** was measured in the presence of the substrate at the several different concentrations in the range of 25 - 200 × 10^{-3} M. For the measurements of the activation energy of decomposition of **3**, the amount of H$_2$O$_2$ was reduced from 1.2 to 0.8 eq to decrease the concentration of free H$_2$O$_2$ in the reaction mixture because catalase activity of **3** strongly affected the rate of decomposition at higher temperatures. The measurements were carried out at -10, -8, -6, and -4°C.

Quantum mechanical calculations

All the DFT calculations were carried out at the spin-unrestricted PBE1KCIS/6-31G* level of theory[24] implemented in the Gaussian09[25] suite of programs. The initial geometries were retrieved from the X-ray crystal structure. The stationary states were confirmed by frequency analysis and the transition state was characterized by one imaginary frequency and their relative motion towards the reactant and product side. The zero-point energy (ZPE) correction was also applied to the energy of all the reported structures.

Aknowledgements

This work was supported by a Grant-in-Aid for Scientific Research B (No. 21350037) from the Ministry of Education, Culture, Sports, Science and Technology, Japan and by "Creating Research Center for Advanced Molecular Biochemistry", Strategic Development of Research Infrastructure for Private Universities, the Ministry of Education, Culture, Sports, Science and Technology, (MEXT) Japan. The author appreciates to Dr. Hiroyasu Sato at Rigaku Corporation for determination of crystal structures of **2a** and **2b**, and to Dr. Shinji Kitao at Kyoto University Research Reactor Institute for measurements of part of the Mössbauer spectra.

Notes and references

[a]*Department of Molecular Chemistry and Biochemistry, Doshisha University, Tatara Miyakotani 1-3, Kyotanabe Kyoto 610-0321, Japan. Fax: (+81) 774-65-6848; Tel: (+81) 774-65-6652; E-mail: mkodera@mail.doshisha.ac.jp*

[b]*Department of Life Science, University of Hyogo, Kouto 2-1, Ako-gun Kamigori-cho Hyogo 678-1297, Japan. Fax: (+81) 791-58-0181; Tel: (+81) 791-58-0181; E-mail: ogura@sci.u-hyogo.ac.jp*

[c]*Graduate School of Informatics and Engineering, The University of Electro-Communications, Chofugaoka 1-5-1, Chofu, Tokyo 182-8585, Japan. Fax: (+81) 42-443-5555; Tel: (+81) 42-443-5555; E-mail: kyoshio@pc.uec.ac.jp*

[d]*Institute for Materials Chemistry and Engineering, Kyushu University, Fukuoka 819-0395, Japan. Fax: (+81) 92-802-2529; Tel: (+81) 92-802-2528; E-mail: kazunari@ms.ifoc.kyushu-u.ac.jp*

† Electronic Supplementary Information (ESI) available: X-ray analysis data of **2a** and **2b**. ESI MS spectra of **2b** and ^{18}O-labeled **2b**. Isotope peaks of the CSI MS spectrum for fully ^{18}O-labeled **3**. Möossbauer spectra of **2a** and the decomposed product of **3**. Oxidation of alkene with H_2O_2 catalyzed by **2b**. See DOI: 10.1039/b000000x/

1 D. M. Kurtz Jr, *J. Biol. Inorg. Chem.,* 1997, **2**, 159.
2 (a) L. Shu, J. C. Nesheim, K. Kauffmann, E. Münck, J. D. Lipscomb, L. Que, *Science*, 1997, **275**, 515; (b) C. E. Tinberg, S. J. Lippard, *Acc. Chem. Res.*, 2011, **44**, 280.
3 W. J. Song, M. S. McCormick, R. K. Behan, M. H. Sazinsky, W. Jiang, J. Lin, C. Krebs, S. J. Lippard, *J. Am. Chem. Soc.*, 2010, **132**, 13582; (b) W. J. Song, S. J. Lippard, *Biochemistry*, 2011, *50*, 5391.
4 L. J. Bailey, B. G. Fox, *Biochemistry*, 2009, **48**, 8932.
5 V. V. Vu, J. P. Emerson, M. Martinho, Y. S. Kim, E. Münck, M. H. Park, L. Que, *Proc. Natl. Acad. Sci. USA*, 2009, **106**, 14814.
6 B. J. Brazeau, R. N. Austin, C. Tarr, J. T. Groves, J. D. Lipscomb, *J. Am. Chem. Soc.*, 2001, **123**, 11831.
7 (a) L. J. Murray, S. G. Naik, D. O. Ortillo, R. García-Serres, J. K. Lee, B. H. Huynh, S. J. Lippard, *J. Am. Chem. Soc.*, 2007, **129**, 14500; (b) A. D. Bochevarov, J. Li, W. J. Song, R. A. Friesner, S. J. Lippard, *J. Am. Chem. Soc.*, 2011, **133**, 7384.
8 (a) I. Siewert, C. Limberg, *Chem.Euro. J.*, 2009, **15**, 10316; (b) S. Friedle, E. Reisner, S. J. Lippard, *Chem. Soc. Rev.*, 2010, **39**, 2768.
9 J. R. Hagadorn, L. Que, W. B. Tolman, *J. Am. Chem. Soc.*, 1998, **120**, 13531.
10 E. C. Carson, S. J. Lippard, *J. Am. Chem. Soc.*, 2004, **126**, 3412.
11 X. Zhang, H. Furutachi, S. Fujinami, S. Nagatomo, Y. Maeda, Y. Watanabe, T. Kitagawa, M. Suzuki, M. *J. Am. Chem. Soc.*, 2005, **127**, 826.
12 S. Friedle, J. J. Kodanko, A. T. Morys, T. Hayashi, P. Moënne-Loccoz, S. J. Lippard, *J. Am. Chem. Soc.*, 2009, **131**, 14508.
13 (a) M. Kodera, M. Itoh, K. Kano, T. Funabiki, M. Reglier, *Angew. Chem. Int. Ed.*, 2005, **44**, 7104; (b) M. Kodera, Y. Kawahara, Y. Hitomi, T. Nomura, T. Ogura, Y. Kobayashi, *J. Am. Chem. Soc.*, 2012, **134**, 13236.
14 (a) J. C. Price, E. W. Barr, B. Tirupati, J. M. Bollinger, and C. Krebs, *Biochemistry*, 2003, **42**, 7497. (b) C. Krebs, D. Galonić Fujimori, C. T. Walsh, and J. M. Bollinger, *Acc. Chem. Res.*, 2007, **40**, 484.
15 (a) J. England, M. Martinho, E. R. Farquhar, J. R. Frisch, E. L. Bominaar, E. Münck, L. Que, *Angew. Chem. Int. Ed.*, 2009, **48**, 3622; (b) J. England, Y. Guo, K. M. Van Heuvelen, M. A. Cranswick, G. T. Rohde, E. L. Bominaar, E. Münck, L. Que, *J. Am. Chem. Soc.*, 2011, **133**, 11880; (c) D. C. Lacy, R. Gupta, K. L. Stone, J. Greaves, J. W. Ziller, M. P. Hendrich, A. S. Borovik, *J. Am. Chem. Soc.*, 2010, **132**, 12188; (d) J. P. Bigi, W. H. Harman, B. Lassalle-Kaiser, D. M. Robles, T. A. Stich, J. Yano, R. D. Britt, C. J. Chang, *J. Am. Chem. Soc.*, 2012, **134**, 1536.
16 G. Xue, A. Pokutsa, and L. Que, *J. Am. Chem. Soc.*, 2011, **133**, 16657.
17 A. Hazell, K. B. Jensen, C. J. McKenzie, H. Toftlund, *J. Chem. Soc., Dalton Trans*., 1993, 3249.
18 A. T. Fiedler, X. Shan, M. P. Mehn, J. Kaizer, S. Torelli, J. R. Frisch, M. Kodera, and L. Que Jr., *J. Phys. Chem. A*, 2008, **112**, 13037.
19 (a) K. Kim, S. J. Lippard, *J. Am. Chem. Soc.*, 1996, **118**, 4914; (b) Y. Dong, Y. Zang, L. Shu, E. C. Wilkinson, L. Que Jr., K. Kauffmann, E. Münck, *J. Am. Chem. Soc.*, 1997, **119**, 12683; (c) M. Kodera, M. Itoh, K. Kano, T. Funabiki, *Bull. Chem. Soc. Jpn.*, 2006, **79**, 252.
20 A. M. Valentine, P. Tavares, A. S. Pereira, R. Davydov, C. Krebs, B. M. Hoffman, D. E. Edmondson, B. H. Huynh, S. J. Lippard, *J. Am. Chem. Soc.*, 1998, **120**, 2190.
21 (a) M. Costas, M. P. Mehn, M. P. Jensen, L. Que, *Chem. Rev.*, 2004, **104**, 939; (b) G. Xue, D. Wang, R. De Hont, A. T. Fiedler, X. Shan, E. Münck, L. Que, *Proc. Natl. Acad. Sci. USA*, 2007, **104**, 20713; (c) G. Xue, A. T. Fiedler, M. Martinho, E. Münck, L. Que, *Proc. Natl. Acad. Sci. USA*, 2008, **105**, 20615.
22 (a) F. A. Chavez, R. Y. N. Ho, M. Pink, V. G. Young, Jr., S. V. Kryatov, E. V. Rybak-Akimova, H. Andres, E. Münck, L. Que, Jr., W. B. Tolman, *Angew. Chem., Int. Ed.*, 2002, **41**, 149; (b) M. Yamashita, H. Furutachi, T. Tosha, S. Fujinami, W. Saito, Y. Maeda, K. Takahashi, K. Tanaka, T. Kitagawa, M. Suzuki, *J. Am. Chem. Soc.*, 2007, **129**, 2; (c) A. T. Fiedler, X. Shan, M. P. Mehn, J. Kaizer, S. Torelli, J. R. Frisch, M. Kodera, L. Que Jr., *J. Phys. Chem. A*, 2008, **112**, 13037.
23 H. Zheng, S. J. Yoo, E. Münck, L. Que Jr., *J. Am. Chem. Soc.*, 2000, **122**, 3789.
24 (a) Y. Zhao, D. G. Truhlar, *J. Chem. Theory Comput.* 2005, **1**, 415; (b) R. Ditchfield, W. J. Hehre, J. A. Pople, *J. Chem. Phys.*, 1971, **54**, 724; (c) W. J. Hehre, R. Ditchfield, J. A. Pople, *J. Chem. Phys.*, 1972, **56**, 2257; (d) V. A. Rassolov, J. A. Pople, M. A. Ratner, T. L. Windus 1998, **109**, 1223.
25 M. J. Frisch, et al., *Gaussian09, Revision C.01*, Gaussian Inc., Wallingford, CT, 2010.